Applied Surface Science 638 (2023) 157982

Contents lists available at ScienceDirect

Applied Surface Science

journal homepage: www.elsevier.com/locate/apsusc

Full length article

Promising anisotropic mechanical, electronic, and charge transport properties of 2D InN alloys for photocatalytic water splitting

Dogukan Hazar Ozbey [a], Mehmet Emin Kilic [b,*], Engin Durgun [a,*]

[a] UNAM-National Nanotechnology Research Center and Institute of Materials Science and Nanotechnology, Bilkent University, Ankara 06800, Turkey
[b] Computational Science Research Center, Korea Institute of Science and Technology, Seoul 02792, Republic of Korea

ARTICLE INFO

Keywords:
InN
2D materials
Photocatalytic water splitting
Nanoelectronics
Optoelectronics

ABSTRACT

Two-dimensional (2D) materials with unique physical properties lead to new possibilities in future nanomaterial-based devices. Among them, 2D structures suitable to be the solar-driven catalyst for water-splitting reactions have become excessively important since the demand for clean energy sources has increased. Apart from the conventional crystals with well-known symmetries, recent studies showed that materials with exotic decorations could possess superior features in these kinds of applications. In this respect, we report novel 2D tetrahexagonal (*th*-) InN crystal and its ordered alloys $In_{0.33}X_{0.67}N$ (X = Al, Ga) that can be utilized as effective catalysts for water splitting reactions. Proposed structures possess robust energetic, dynamical, thermal, and mechanical stability with a versatile mechanical response. After a critical tensile strain value, all monolayers exhibit strain-induced negative Poisson's ratio in a particular crystal direction, making them half-auxetic materials. The examined materials are indirect semiconductors with desired band gaps and band edge positions for water-splitting applications. Due to their structural anisotropy, they have direction-dependent mobility that can keep the photogenerated charge carriers separated by reducing their recombination probability, which boosts the photocatalytic process. High absorption capacity in the wide spectral range underlines their potential performance. The versatile mechanical, electronic, and optical properties of 2D *th*-InN and its alloys, together with their remarkable structural stability, indicate that they can appropriately be exploited in the future for water splitting applications.

1. Introduction

In condensed matter physics, graphene can be viewed as the most celebrated material after its first successful exfoliation [1,2] and paved the way for a remarkable scientific research area called two-dimensional (2D) materials. Since its isolation in 2004, many other 2D materials, often called "post-graphene crystals", have been discovered and thoroughly investigated [3–7]. In addition to these materials, numerous 2D carbon allotropes have been examined by intensive theoretical and experimental studies since it is known that alteration in the configuration of existing structures can bring about novel or superior features that could be practically utilized in nanoscale applications [8–11]. One of the very recent examples of these allotropes is tetrahexagonal carbon (*th*-C), which is obtained by performing Stone–Wales transformation to penta-graphene [12]. The suggested structure, which has an anisotropic buckled configuration with periodically arranged tetragonal (t) and hexagonal (h) rings, has been confirmed to be dynamically and thermally stable [13]. Furthermore, the *th*-C has been revealed to be a direct band gap (2.63 eV) semiconductor with high charge carrier mobility, and auxetic mechanical response, namely sign-tunable Poisson's ratio [14,15]. The exciting properties resulting from this new 2D arrangement of carbon atoms have prompted significant attention from the scientific community and paved the way for studies extending to other carbon-based 2D systems. For instance, *th*-CN_2 monolayer has been predicted to be an insulating, stiff material with in-plane Young's modulus of 340 N m^{-1} similar to that of graphene (340 ± 50 N m^{-1} [16]) and exhibits negative Poisson's ratio (NPR) [17]. With their comprehensive study, Kilic et al. have theoretically investigated the robustness of 2D group-IV *th*-carbide structures and have underlined their remarkable anisotropic mechanical, electronic, and optical properties in the scope of photocatalytic water-splitting application [18,19]. Moreover, following the prediction of monolayer and bilayer of *th*-GeC_2 that possess high-anisotropic mobility and thermodynamic stability [20], their electronic properties and carrier transport characteristics in the ballistic regime (sub-10 nm) have been revealed to be utilizable in nanoelectronics applications [21]. Considering the exciting results suggested in mentioned studies, it can be inferred that unique *th*-

* Corresponding authors.
E-mail addresses: mekilic@kist.re.kr (M.E. Kilic), durgun@unam.bilkent.edu.tr (E. Durgun).

https://doi.org/10.1016/j.apsusc.2023.157982
Received 17 March 2023; Received in revised form 3 July 2023; Accepted 5 July 2023
Available online 11 July 2023

morphology can evoke the emergence of unexpected properties absent in existent forms of the well-known monolayers.

The ongoing research in this area led to a question of whether other materials can also be obtained in the *th*-form. To answer this question, the stability of various 2D materials that are iso-structural to *th*-C has been examined and reported to possess a wide variety of properties. For instance, 2D *th*-BN has been revealed to be a stable and semiconducting material with a wide band gap that can be tuned by strain engineering and hydrogenation [22]. Additionally, the *th*-BN has been predicted to have high optical absorption in the ultraviolet region rendering it a promising material for optoelectronic applications. Furthermore, it has been reported that 2D AlN is also stable in *th*-form and exhibits remarkable properties such as high, anisotropic carrier mobility with suitable band edge positions, which makes it an ideal catalyst for visible light water-splitting reactions [23]. In contrast, efforts to find a stable conformation have been restricted to the *h*-structure among the three possible arrangements of 2D-InN since the tetragonal and V-shaped structures have been revealed to have imaginary frequencies in their phonon spectra, indicating a lack of stability [24].

Mentioned theoretical findings have strengthened the possibility of the existence of stable 2D *th*-InN crystal and made an essential contribution to our motivation to investigate its pristine and alloyed derivatives. In this work, we design *th*-InN monolayer and its ordered alloys (*th*-$In_{0.33}X_{0.67}N$ (X = Al, Ga)) and unveil their effective photocatalytic performance in the framework of *ab initio* calculations. Following the determination of ground-state configurations, we obtain their dynamical, thermal, and mechanical stability with phonon spectrum analysis, *ab initio* molecular dynamics (AIMD) simulations, and elastic stability criteria, respectively. Next, we show the anisotropic and auxetic mechanical responses of these materials. Subsequent to examining the electronic properties, we evaluate their photocatalytic water-splitting capacity in terms of unstrained and strain-dependent band edge positions. Finally, we explore the optical response of the proposed systems.

2. Methods

All the calculations throughout this computational study were based on density functional theory (DFT) implemented in the Vienna *Ab initio* Simulation Package (VASP) [25–28]. To define the potentials of all the constituent elements of *th*-$In_{0.33}X_{0.67}N$ (X = Al, Ga, In) structures, the projector augmented wave (PAW) [29,30] method was employed. The exchange–correlation potential was approximated within the generalized gradient approximation (GGA) using the Perdew, Burke, and Ernzerhof (PBE) functional [31]. The correction to the underestimated electronic band gaps resulting from the GGA-PBE was assured by the Heyd–Scuseria–Ernzerhof hybrid functional (HSE06) [32,33], constructed by 25% of nonlocal Fock exchange, 75% of PBE exchange, and 100% of PBE correlation energy. The energy cutoff value of 520 eV was taken for the plane-wave basis set. The Brillouin Zone (BZ) was sampled by the Γ-centered 24 × 24 × 1 uniform k-point mesh. To hinder any artificial interactions, a vacuum space of 20 Å was placed along the non-periodic z-axis, and periodic boundary conditions were applied for the x- and y-axis. The atomic positions were optimized until the force on each atom was less than 0.01 eV/Å. The convergence criteria for electronic and ionic steps were set to 10^{-5} eV and 10^{-4} eV, respectively. The dynamic stability of the examined monolayers was determined by the phonon spectrum analyses, and the calculations were performed using the finite displacement method implemented in the PHONOPY package for 4 × 3 × 1 supercell [34] with increased accuracy (i.e., 10^{-8} eV and 10^{-4} eV/Å for energy and force convergence, respectively). The thermal stability of the structures was tested throughout AIMD calculations with 4 × 3 × 1 supercell for 6 ps of total simulation time with a time step of 1 fs using Nose–Hoover thermostat [35]. To reveal the optical response of the monolayers, the random-phase approximation [36] (RPA) on top of single-shot GW (G_0W_0) [37] with 8 × 8 × 1 k-point mesh, 480 eV cutoff energy, and 160 total number of bands was adopted. For the optical response including many-body effects, the Bethe–Salpeter equation (BSE) [38,39] was solved within the Tamm–Dancoff approximation following the G_0W_0 step.

3. Results and discussion

3.1. Atomic structures

We began by presenting the structural properties of *th*-InN monolayer and its ordered alloys (*th*-$In_{0.33}X_{0.67}N$ (X = Al, Ga)). In 2D materials, alloying can significantly affect the material's overall properties and performance, making them useful for various applications. Alloyed monolayers can exist in a variety of configurations, each with its own set of properties and characteristics. While they have in general random configurations, they can also include clusters with distinct shapes (e.g., triangular, square, and circular), as well as lines in various forms. Here, we are inspired by an experimental study in which ordered alloys of the MoS_2 monolayer have been obtained by substituting the S atoms directionally with Se atoms under electron irradiation [40]. As the unit cell of the *th*-InN crystal consists of six In and six N atoms, we designed a specific alloy configuration (depicted in Fig. 1(a)) by substituting four In atoms with Al and Ga atoms, resulting in an ordered alloy with a distinct pattern that imposes a particular concentration of elements. For the sake of convenience and to facilitate the comparisons, we abbreviate all the structures as *th*-$In_{0.33}X_{0.67}N$ (X = Al, Ga, In) where X = In refers to the pristine *th*-InN monolayer. While the geometry of *th*-InN belongs to the *Pccm* space group (point group of D_{2h}), it transforms to the *Pma2* (point group of C_{2v}) for alloys. Pristine and alloyed structures possess a conventional orthorhombic lattice with **a** and **b** lattice constants. The unit cell comprises sp^2 hybridized 3-fold coordinated (N^3 and X^3), and sp^3 hybridized 4-fold coordinated atoms (N^4 and In^4) as shown in Fig. 1(a). The combination of trigonal pyramidal geometry consisting of N^3 and X^3 atoms and tetrahedral geometry consisting of N^4 and In^4 atoms give rise to a buckled configuration with three sublayers. The middle layer is only occupied by 4-coordinated atoms, while 3-coordinated ones form the top and bottom layers. We define two buckling thicknesses which are the vertical distance between N^3 atoms (h_1) and between X^3 atoms (h_2). In addition bond lengths of N^3-X^3, X^3-N^4, and N^3-In^4 are identified by d_1, d_2 and d_3, respectively. The optimized structural parameters for *th*-$In_{0.33}X_{0.67}N$ monolayers **a**, **b**, h_1, h_2, d_1, d_2 and d_3 are summarized in Table 1. It can be noted that the increasing atomic number of X atoms results in larger lattice constants **a** and **b**. Correspondingly, bond lengths and buckling heights of the structures show elongation in the same manner.

3.2. Stability

To check the energetics and stability of *th*-InN monolayer, we started with determining the corresponding local minima on the potential energy surface of the 2D and 3D InN materials with the same stoichiometry. We calculate total energy per atom with respect to normalized unit cell area (A/A_0) for 2D and unit cell volume (V/V_0) for 3D allotropes as given in Fig. 1(b). Here, A_0 and V_0 denote the equilibrium lattice area and volume, respectively. As expected, all of the 2D structures have higher total energies compared to their 3D counterparts. On the other hand, while *th*-InN has higher total energy than *h*-InN, it is calculated to be more energetic than *t*-InN, which has been shown as unstable in the literature [24]. The energy lowering can be regarded as the first indicator of the stability of *th*-InN. In addition, the formation energy difference between a 2D material and its reference bulk structures can be another preliminary test for the stability of the monolayers. A low formation energy implies that realizing the proposed 2D system is plausible. To calculate the difference in formation energies, we use the expressions of $\Delta E_{\mathbf{c}} = E^{th}_{2D} - E^{c}_{3D}$ for 3D cubic zinc blend and, $\Delta E_{\mathbf{h}} = E^{th}_{2D} - E^{h}_{3D}$ for 3D hexagonal systems, where E^{th}_{2D}, E^{c}_{3D} and

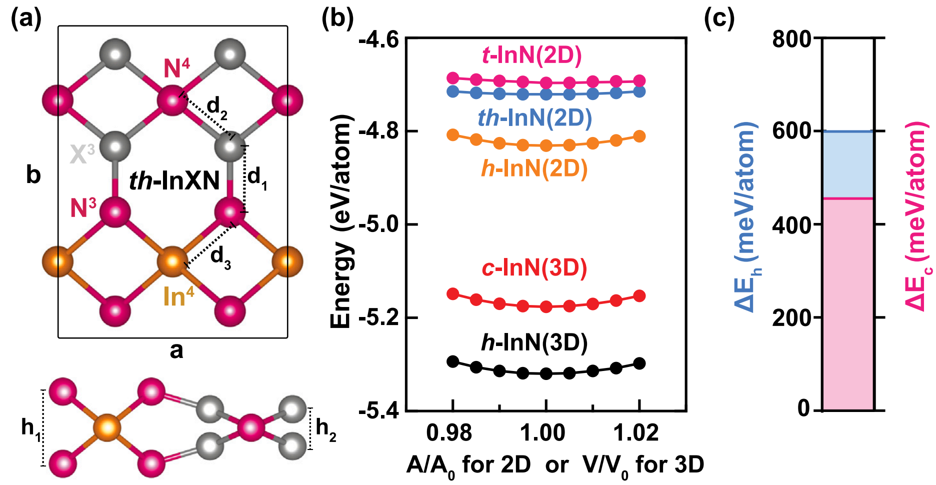

Fig. 1. (a) Top and side views of *th*-$In_{0.33}X_{0.67}N$ (X = Al, Ga, and In) monolayers. (b) The total energy per atom with respect to normalized unit cell area (A/A_0) for 2D and unit cell volume (V/V_0) for 3D allotropes. (c) The formation energy difference of *th*-InN with respect to its cubic zinc blende (*c*-InN) and hexagonal (*h*-InN) bulk forms (painted by pink and blue colors, respectively).

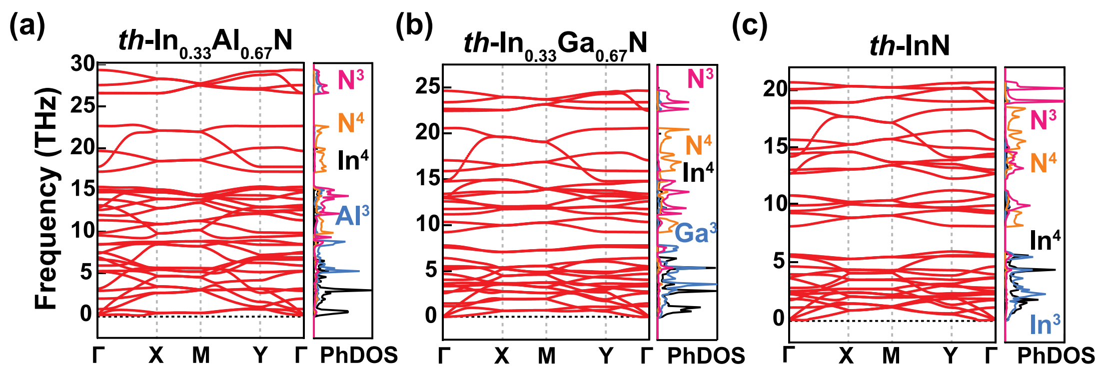

Fig. 2. Calculated phonon dispersions and phonon density of states (PhDOS) of (a) *th*-$In_{0.33}Al_{0.67}N$ (b) *th*-$In_{0.33}Ga_{0.67}N$, and (c) *th*-InN monolayers.

Table 1
Calculated lattice parameters **a** and **b**, bond lengths d_1 for X^3-N^3, d_2 for X^3-N^4, and d_3 for N^3-In^4, thickness (or buckling height) h_1 and h_2, the electronic band gap energy E_g^{HSE} with HSE06 functional method, and the type of electronic band (Type).

	a (Å)	**b** (Å)	d_1 (Å)	d_2 (Å)	d_3 (Å)	h_1 (Å)	h_2 (Å)	E_g^{HSE} (eV)	Type
th-$In_{0.33}Al_{0.67}N$	5.83	8.18	1.74	1.94	2.18	2.05	1.05	2.19	Indirect
th-$In_{0.33}Ga_{0.67}N$	6.00	8.26	1.82	2.03	2.19	2.18	1.24	1.90	Indirect
th-InN	6.35	8.98	2.04	2.23	2.21	2.15	1.44	1.08	Indirect

E^c_{3D} denotes energy per atom for 2D *th*-InN, 3D *c*-InN and 3D *h*-InN structures, respectively. The calculated values of ΔE_c (455 meV/atom) and ΔE_h (599 meV/atom) are illustrated in Fig. 1(c). Comparing with the $\Delta E = 823$ meV/atom of already-synthesized 2D graphdiyne [41], it can be inferred that 2D *th*-InN has the potential to be fabricated by experimental techniques.

The investigation of phonon modes can provide a hint about the dynamical stability of crystals. Additionally, the phonon density of states (PhDOS) calculated from the phonon dispersion gives insight into the distribution of phonon frequencies. To inspect these, we calculated the phonon dispersion spectra of *th*-$In_{0.33}X_{0.67}N$ monolayers by the frozen-phonon technique, which uses the quadratic dependence of the total energy to the displacement of ions. Phonon dispersion curves throughout the BZ and related atom-projected PhDOS of examined monolayers are given in Fig. 2. It is found that all phonon modes of *th*-$In_{0.33}X_{0.67}N$ crystals have real frequencies, which points out the structural integrity. The PhDOS results show that, in all of the monolayers, the vibrations of N^3 atoms give rise to the highest frequencies, which can be attributed to their atomic mass being the lightest. Similarly, the second-highest phonon frequencies are caused by the vibrations of N^4 atoms. The maximum of the vibrational frequencies, which is also related to the mechanical properties of a crystal, tend to increase when the atomic radius of the X element decreases. This trend is generally seen as an indication of an improvement in bond strength. Going down in group-III, the distance between atoms in the crystal lattice decreases, leading to stronger bonding and higher vibrational frequencies. On the other hand, since realistic experimental conditions such as lattice mismatch between two structures, substrate effects, or bending can induce a strain on 2D materials, their endurance under the mentioned effects should be tested. To examine that, we performed phonon dispersion calculations while equi-biaxial tensile strain (up to 10%) was imposed on the monolayers. The resulting vibrational frequencies of strained structures are also real, which can be seen in Figure S1. These findings show that *th*-$In_{0.33}X_{0.67}N$ crystals maintain their robustness even they are subjected to a high degree of strains.

High-temperature stability of 2D *th*-$In_{0.33}X_{0.67}N$ crystals was investigated through AIMD simulations at elevated temperatures up to 900 K. The variation of the total energy of the monolayers during the total simulation time of 6 ps is given in Fig. 3, and snapshots of the structures at the end of the calculation are displayed as inset.

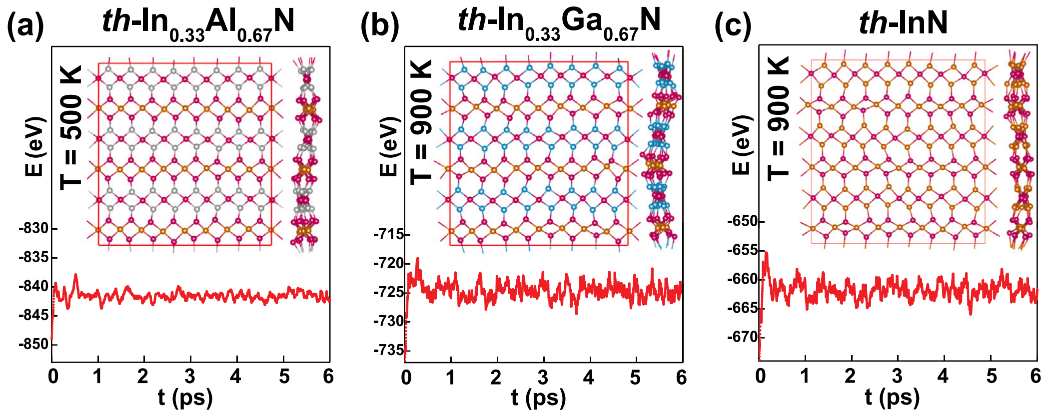

Fig. 3. The evolution of total energy during the AIMD simulations (lower part) and the snapshots of the structure from top and side views at the end of the simulation time (inset) for (a) *th*-$In_{0.33}Al_{0.67}N$ (b) *th*-$In_{0.33}Ga_{0.67}N$, and (c) *th*-InN monolayers. The maximum temperature used for simulations is indicated in the corresponding plots for each structure.

Minute fluctuations of total energy with respect to equilibrium value in conjunction with the ultimate configuration of the structures confirm the thermal stability of *th*-$In_{0.33}X_{0.67}N$ monolayers. Apart from the overall integrity, the evolution of total energy without any distinct drop signifies that no phase transition occurred during the entire simulation.

To validate strain-induced mechanical stability, we utilized Born-Huang elastic stability criteria [42] by using the in-plane elastic constants C_{ij} of a given material and relations $C_{11}C_{22}-C_{12}^2>0$ and $C_{66}>0$. The values of C_{ij} can be determined from strain energy per unit area (E_s), which corresponds to the difference between the total energy of the strain-free crystal and its axially strained variations. The E_s of *th*-$In_{0.33}X_{0.67}N$ monolayers is calculated by the following expression of in-plane strains:

$$E_s(\varepsilon)=\frac{1}{2}C_{11}\varepsilon_x^2+\frac{1}{2}C_{22}\varepsilon_y^2+C_{12}\varepsilon_x\varepsilon_y+2C_{66}\varepsilon_{xy}^2 \tag{1}$$

where ε_x, ε_y and ε_{xy} are the values of uniaxial strain in *x*-, *y*-directions and biaxial strains, respectively. To obtain the strain energy plots for uniaxial, biaxial, and shear strains (given in Figure S2), we applied different types of strains with values ranging from −2% to +2% with 0.5 increments. It should be noted that the atomic positions are relaxed after implementing strain. According to the calculated C_{ij} values, the Born-Huang criteria are found to be fulfilled, and mechanical stability of *th*-$In_{0.33}X_{0.67}N$ structures is confirmed in addition to dynamical and thermal stability.

3.3. Mechanical properties

After revealing the structural stability of proposed monolayers, we explored their mechanical response in terms of angle-dependent in-plane stiffness ($Y^{2D}(\Theta)$) and Poisson's ratio ($\nu(\Theta)$). Since the structural anisotropy in 2D materials leads to different behavior in distinct crystal orientations, the study of angle-dependency of mechanical properties is of great importance. To reveal that, the mechanical response of monolayers was determined through the use of the calculated nonzero elastic constants C_{ij}, as revealed by the corresponding relations [43,44]:

$$Y^{2D}(\Theta)=\frac{A}{C_{11}\ s^4\ +\ C_{22}\ c^4\ +\ (B\ -\ 2\ C_{12})\ c^2\ s^2} \tag{2}$$

$$\nu(\Theta)=-\frac{(C_{11}\ +\ C_{22}\ -\ B\ )\ c^2\ s^2\ -\ C_{12}\ (c^4\ +\ s^4)}{C_{11}\ s^4\ +\ C_{22}\ c^4\ +\ (B\ -\ 2\ C_{12})\ c^2\ s^2} \tag{3}$$

where $c=\cos(\theta)$, $s=\sin(\theta)$, $A=\ (C_{11}C_{22}-C_{12}^2)$, and $B=\ A/C_{66}$.

$Y^{2D}(\Theta)$ is a measure of elasticity that is governed by the crystalline structure, which is analogous to Young's modulus of bulk materials. For *th*-$In_{0.33}X_{0.67}N$ monolayers, the variation of calculated Y^{2D} as a function of in-plane angle Θ is given in polar diagrams in Fig. 4.

Table 2
Calculated in-plane Young's modulus (Y_x^{2D} and Y_y^{2D}) in N/m, Poisson's ratio (ν_x and ν_y), and threshold values of negative Poisson's ratio (NPR_x and NPR_y) in *x*- and *y*-directions for *th*-$In_{0.33}X_{0.67}N$ monolayers. Y_x^{2D}, Y_y^{2D}, ν_x, and ν_y values were determined at small strain region range from −2 to +2% while the NPR_x and NPR_y were calculated at relatively large strain range from −2% to +10%.

	Y_x^{2D} (N/m)	Y_y^{2D} (N/m)	ν_{xy}	ν_{yx}	NPR_x	NPR_y
th-$In_{0.33}Al_{0.67}N$	85	61	0.03	0.03	–	2%
th-$In_{0.33}Ga_{0.67}N$	75	53	0.08	0.05	–	5%
th-InN	59	41	0.04	0.06	–	4%

The resulting plots show that the mechanical behavior of the examined materials is strongly direction-dependent. The corresponding in-plane stiffness values of examined monolayers along *x*- ($\Theta=0$) and *y*- ($\Theta=90$) directions (given as Y_x^{2D} and Y_y^{2D}, respectively) are summarized in Table 2. $\Theta=0$ and $\Theta=90$ cases correspond to zigzag and armchair directions, respectively. Considering the recently reported Y^{2D} of *th*-C [14] ($Y_x^{2D}=286$ N/m and $Y_y^{2D}=279$ N/m) and group-IV *th*-carbides [18] (ranging between 99 to 143 N/m for Y_x^{2D} and 66 to 107 N/m for Y_y^{2D}), *th*-$In_{0.33}X_{0.67}N$ monolayers have lower values which indicate their relative flexibility. Furthermore, the results also indicate the influence of alloying on the mechanical properties, which can be seen through the variations in the calculated Y^{2D} values in Table 2. It can be observed that as the atomic radius of the *X* elements increases, the stiffness values alter in descending order, aligning with previous vibrational results, indicating that the monolayers with shorter bonds are more robust [45].

Next, the Poisson's ratio (ν), which can be defined as the ratio of the transverse deformation to the deformation perpendicular to that specific direction, is calculated, $\nu(\Theta)$ of *th*-$In_{0.33}X_{0.67}N$ is given in Fig. 4 (lower panel). Although a similar anisotropic behavior is observed in the ν profile, it takes the lowest values in the *x*- and *y*-directions as opposed to $Y^{2D}(\Theta)$. In these directions, small values of the ν indicate that all the monolayers are brittle [46] and not able to allow huge dislocations in their atomic arrangements. On the other hand, ν values of all monolayers increase and become more ductile at median angles with respect to principal axes. The physical mechanism behind the anisotropic mechanical response can be correlated to the two inequivalent atomic sites with 3- and 4-fold coordinated atoms (Figure S3–S5). The 3-fold coordinated atoms (X^3 and N^3) only lie in the *y*-direction as shown in Fig. 1, resulting in strong anisotropy. Similar characteristics are also noticed in monoatomic *th*-systems [13,14].

Solid materials that possess negative Poisson's ratio (NPR) are rarely found in nature and are introduced as *auxetic* materials [47]. The uniqueness of materials with NPR emerges from their counter-intuitive

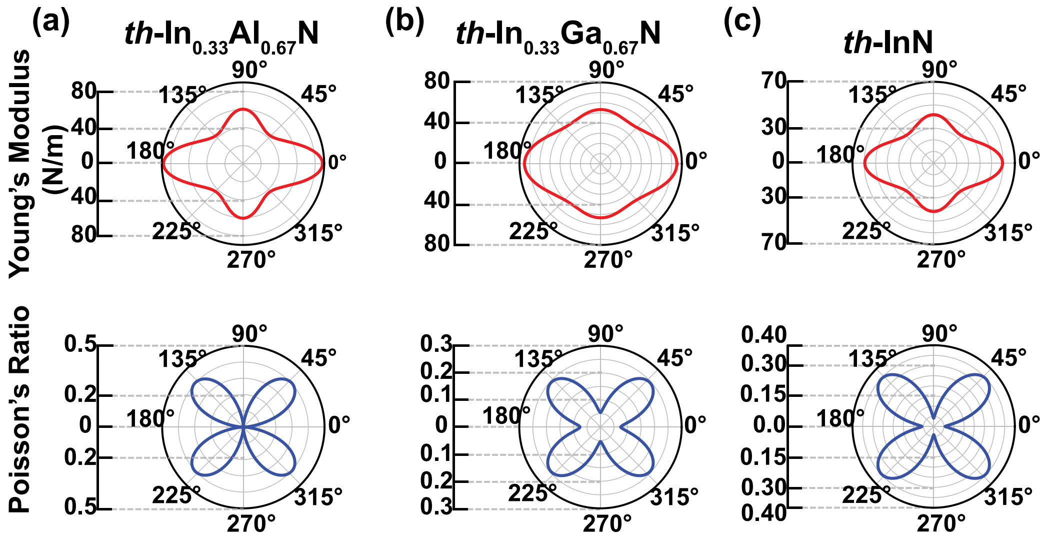

Fig. 4. The angle-dependent in-plane stiffness (upper panel) and Poisson's ratio (lower panel) of (a) *th*-$In_{0.33}Al_{0.67}N$ (b) *th*-$In_{0.33}Ga_{0.67}N$, and (c) *th*-InN monolayers.

mechanical behavior in that the external load in one direction causes the same type of deformation (extension or tension) in another direction. The auxeticity in 2D materials can also be categorized into various classes. For instance, some structures possess this property along different crystal orientations [48,49] while others only show auxetic response in a particular direction [50]. Furthermore, materials can exhibit half-auxetic function, which means they always expand in one direction irrespective of whether they are compressed or pulled in the perpendicular direction [51,52]. More interestingly, some crystals can show a transition from positive to negative Poisson's ratio when a critical value of strain is induced [53]. As it is discussed above, *th*-$In_{0.33}X_{0.67}N$ monolayers do not have intrinsic auxeticity. In order to inspect the possible auxetic phenomena under strain, we systematically investigated the proposed monolayers in the range of −2% to +10% strain levels. We use the finite-difference method [54,55], and the nonlinear lattice behavior due to the imposed axial strain is considered. In this context, v_{xy} represents the ratio of extension or tension in the x-direction to the applied axial strain in the y-direction (in a similar manner, v_{yx} denotes the reciprocal case) and is calculated by the following expression [43,44]:

$$v_{xy} = \left[\frac{\varepsilon_y^{i+1} - \varepsilon_y^{i-1}}{\varepsilon_x^{i+1} - \varepsilon_x^{i-1}} \right] \quad (4)$$

where $i = 1, 2, \ldots$ denotes the successive increment of the applied strain. The alteration of transverse strain and Poisson's ratio with respect to the imposed longitudinal (uniaxial-x or uniaxial-y) tensile strain is plotted in Fig. 5. We found that the examined monolayers show NPR under axial strains only in the y-direction, given in blue colors in Fig. 5. Furthermore, they exhibit a transition from normal to a half-auxetic phase when a critical value of strain (NPR_y in Table 2) is induced. Similar extraordinary direction-dependent, half-auxetic behavior is also observed in graphene [56,57].

3.4. Electronic and photocatalytic properties for water splitting

To inspect the electronic properties of 2D *th*-$In_{0.33}X_{0.67}N$, we examined the electronic band structure, related partial density of states (pDOS), and charge distributions at conduction band minimum (CBM) and valence band maximum (VBM). The obtained electronic band gap energies are listed in Table 1, and band dispersions are illustrated with their corresponding charge densities in Fig. 6. *th*-InN, *th*-$In_{0.33}Ga_{0.67}N$ and *th*-$In_{0.33}Al_{0.67}N$ crystals are found to be indirect semiconductors with 1.08, 1.90 and 2.19 eV band gaps which widen as going up in the X-group, respectively. It means alloying shifts the band gap of the pristine *th*-InN monolayer from the infrared to the visible range. While the CBM of all structures is located at Γ point, VBM's are positioned amid X-Γ direction. The highest valence band is nearly flat in the band structure of pristine and alloyed monolayers, which indicates that the holes in that structures have low mobility. The charge density contour plots belonging to VBM and CBM can be seen in the lower panel, which shows that localization of the charge density is much more pronounced on N^3 and X^3 atoms. In addition, the calculated pDOS results (given in Figure S6) validate that a significant contribution to the electronic states arises from p_z orbitals of these 3-folded N and X atoms.

2D materials and their heterostructures are intrinsically advantageous in photocatalytic water-splitting applications [58–63]. However, a 2D semiconductor should fulfill certain conditions which render it an efficient photocatalyst. The ability to generate free charge carriers and their migration capacity determines the suitability of 2D materials for solar water-splitting applications. In this manner, the electronic properties of 2D materials play a decisive role. Firstly, the semiconductor's band gap should be larger than 1.23 eV, which is the minimum Gibbs free energy that is essentially required to split the water into its constituents. Considering the 2D *th*-$In_{0.33}X_{0.67}N$ structures, while the *th*-InN does not meet the band gap criterion, its alloyed derivatives are convenient to be a prospective catalyst. Additionally, band edges of proposed materials should straddle the redox potentials of water, which is determined by Nerst equations [64] given as: $E_{H^+/H_2} = (-4.44 + pH \times 0.059)$ eV and $E_{O_2/H_2O} = (-5.67 + pH \times 0.059)$ eV. To explore the suitability of the monolayers regarding this condition, we aligned the band edges determined by the HSE functional to the vacuum level (which is obtained from the planar-averaged potential of the 2D system plotted along its surface normal), given in Fig. 7. The redox potentials of water splitting are depicted in green dashed lines for pH = 7, considered to be the pH level of neutral water. The results indicate that *th*-$In_{0.33}Ga_{0.67}N$ monolayer satisfies the band gap criterion and can be used in oxygen evolution reactions (OER), but can only take part in hydrogen evolution reactions (HER) in acidic mediums. On the other hand, the most significant improvement is obtained by the inclusion of Al in *th*-InN since *th*-$In_{0.33}Al_{0.67}N$ monolayer becomes operable for both OER and HER in a practical pH range (i.e., pH = 5–9). This makes 2D *th*-$In_{0.33}Al_{0.67}N$ photocatalytically active for the simultaneous production of hydrogen and oxygen under ambient conditions.

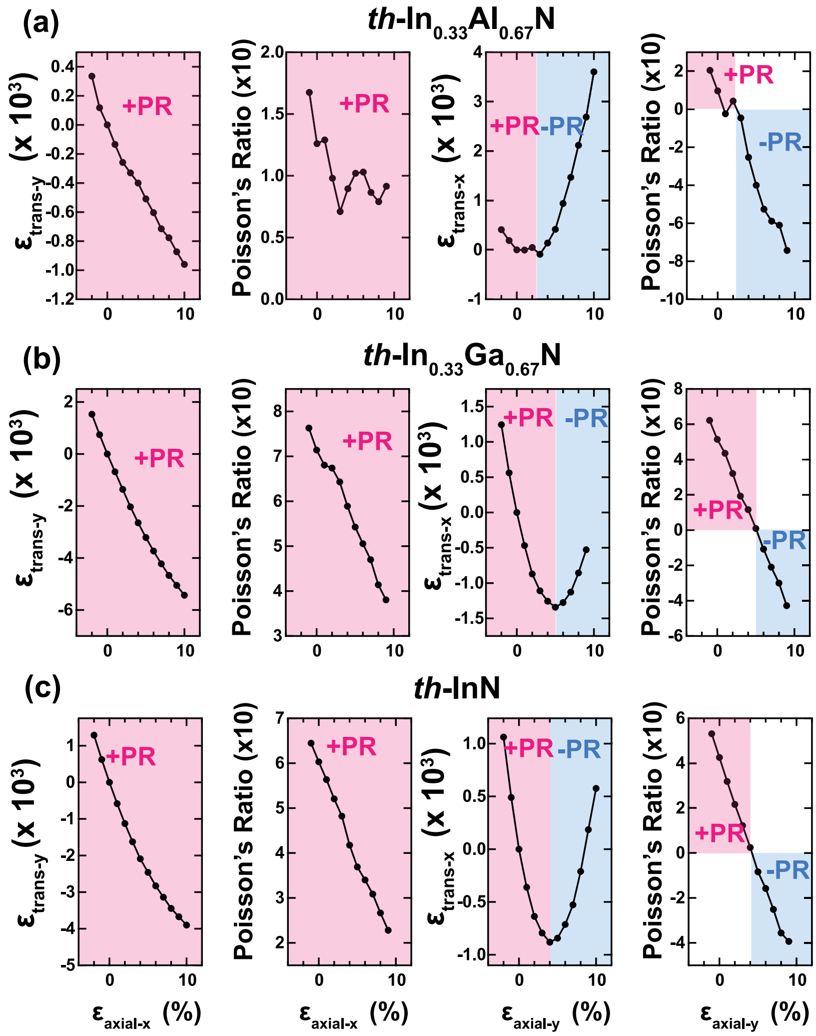

Fig. 5. Variation of transverse strain and Poisson's ratio of (a) *th*-$In_{0.33}Al_{0.67}N$ (b) *th*-$In_{0.33}Ga_{0.67}N$, and (c) *th*-InN monolayers with respect to given longitudinal tensile strain (uniaxial-x and uniaxial-y). The positive (+PR) and negative Poisson's ratio (-PR) is shaded in pink and blue, respectively.

It is noted that the position of the VBM of *th*-InN, and its alloyed structures is much lower than the oxidation potential of O_2/H_2O, indicating that they have an adequate driving force for the OER reaction. However, the CBM energies are not more negative (only 0.16/0.57 eV higher at pH = 0/7 for *th*-$In_{0.33}Al_{0.67}N$)) than the hydrogen reduction potential, which may result in a low catalytic activity. To evaluate the hydrogen evolution reaction, we investigated the Gibbs free energy of hydrogen adsorption (ΔG_{H^*}). For an ideal catalyst, the ΔG_{H^*} should be close to zero [65], and defined as

$$\Delta G_{H^*} = E_{ads} + \Delta E_{ZPE} - T\Delta S_{H^*} \tag{5}$$

where E_{ads} is the hydrogen binding energy, which is calculated relative to the hydrogen molecule as

$$E_{ads} = E_{monolayer+H} - E_{monolayer} - \frac{1}{2}E_{H_2} \tag{6}$$

where $E_{monolayer+H}$ and $E_{monolayer}$ are the total energy of the monolayer with and without H, respectively. E_{H_2} is the total energy of H_2 molecule in the gas phase. Here, ΔE_{ZPE} is the change in zero-point energy between the adsorbed state and gas phase. ΔS_{H^*} is the difference of entropy between the adsorption state of hydrogen and gas phase. The predicted $\Delta E_{ZPE} - T\Delta S_{H^*}$ value at $T = 300$ K is about 0.24 eV [66].

To examine the ΔG_{H^*}, we first calculated the hydrogen adsorption energy on different sites of InN and its alloyed structures. The total energy calculations reveal that the top sites of N^3 are energetically most favorable for the hydrogen adsorption. The obtained binding energy values are −0.92, −1.16, and −1.68 eV for $In_{0.33}Al_{0.67}N$, $In_{0.33}Ga_{0.67}N$, and InN monolayers, respectively. The high negative adsorbed energy values mean that the hydrogen molecule will be adsorbed spontaneously over the corresponding structures. Next, we calculated the ΔG_{H^*} as 0.75, 0.89, and 1.42 eV. The ΔG_{H^*} of 0.75 eV for $In_{0.33}Al_{0.67}N$ is lower than that of $PdSe_2$ [67] and comparable to that of Janus WSSe [68]. Although the ΔG_{H^*} of $In_{0.33}Al_{0.67}N$ is not close to zero, the external potential of 0.16/0.57 eV supplied by photoexcited electrons induces a lower free energy, which tends to spontaneously trigger the HER.

Considering the practical applications, a catalyst that preserves its functionality under strain conditions is of great importance, as imposed strain can alter the band edge positions and band gap energies of the semiconducting systems. To elucidate the effect of strain on electronic properties, we investigated strain-imposed band edges and band gaps of 2D *th*-$In_{0.33}X_{0.67}N$ structures, as shown in Fig. 8. It is found that all the monolayers possess tunable band gaps under different types of applied strain (uniaxial-*x*, uniaxial-*y*, and biaxial). The band gap narrows (widens) with tensile (compressive) strain and the effect is more significant for the tensile case. Considering the band edge positions, it can be inferred that *th*-$In_{0.33}Ga_{0.67}N$ crystal maintains its performance in a reasonable strain range and additionally can be utilized in HER

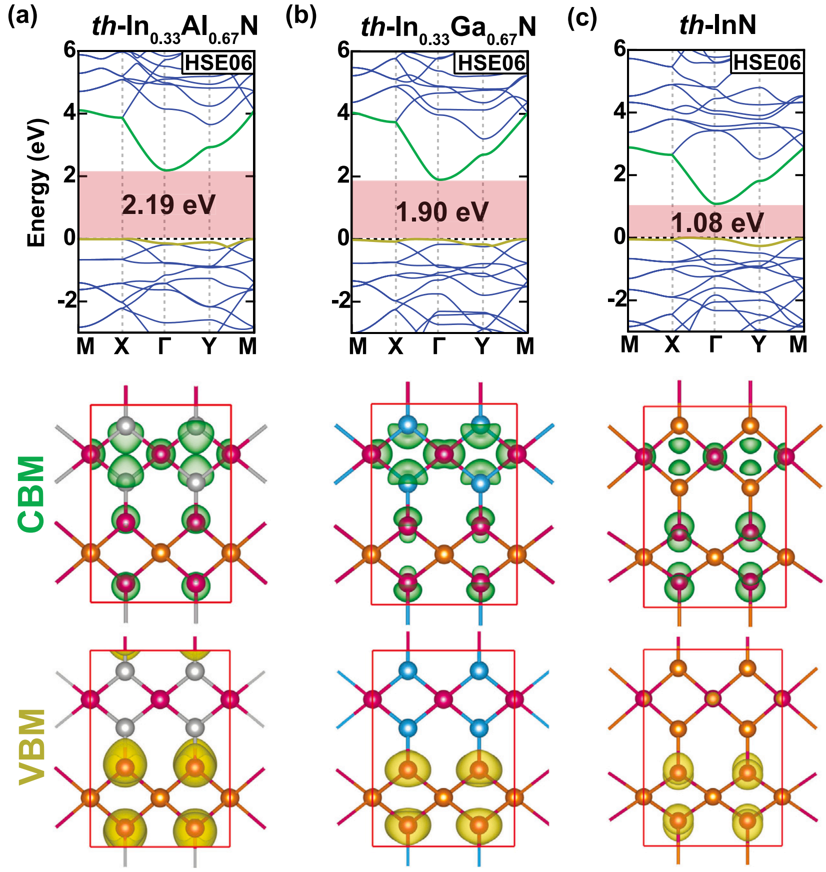

Fig. 6. Upper panel: Electronic band structure of 2D *th*-$In_{0.33}X_{0.67}N$ calculated using the HSE06 functional (the Fermi energy is set to zero and depicted by the dashed black line). and Lower panel: Charge density of CBM (green line) and VBM (yellow line) of 2D of (a) *th*-$In_{0.33}Al_{0.67}N$ (b) *th*-$In_{0.33}Ga_{0.67}N$, and (c) *th*-InN monolayers. The iso-surface of the charge density (green and yellow color lobes) is 0.005 e/Å^3. The gray, blue, pink, and orange balls represent Al, Ga, N, and In atoms, respectively.

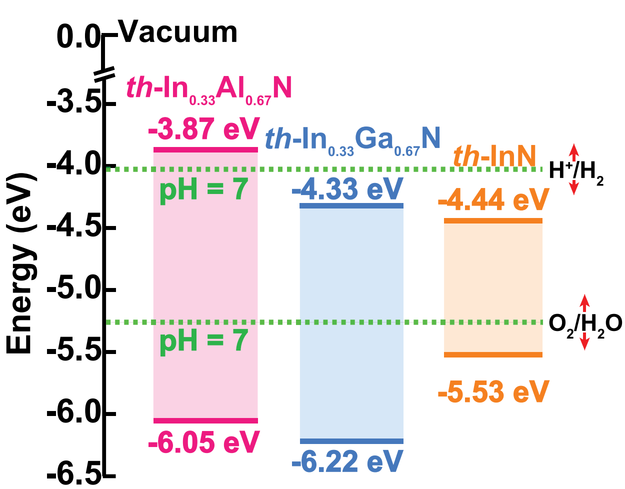

Fig. 7. Location of band edges (CBM and VBM) of 2D *th*-$In_{0.33}X_{0.67}N$ with respect to vacuum level calculated with HSE06 functional. The redox potentials of water splitting are shown in the green dashed line for pH = 7.

under compressive strain for pH < 7. The same situation also holds for *th*-$In_{0.33}Al_{0.67}N$ monolayer, where it can still be employable for both HER and OER reactions within extended strain levels with additional photocatalytic capability in basic environments (pH > 7).

Due to their 2D composition, semiconducting monolayers reduce the distance that photogenerated electrons and holes must travel before reaching the solid/water contact, lowering the chance of electron–hole recombination and potentially improving photocatalytic efficiency. As electrons and holes participate in the photocatalytic operation separately by the hydrogen reduction, $2H^+ + 2e^- \rightarrow H_2$ and oxidation, $H_2O + 2h^+ \rightarrow 1/2\ O_2 + 2H^+$ reactions, any mechanism inhibiting the recombination of these charge carrier particles and ensuring a sufficiently long lifetime is highly desirable. One of the mechanisms utilized in this manner can be anisotropy in electronic transport properties. The different characteristics of electronic band dispersions of VBM and CBM between particular directions indicate that *th*-$In_{0.33}X_{0.67}N$ monolayers possess anisotropic transport features, which increase their potential to be a suitable catalyst. To quantitatively investigate the anisotropy in electron and hole transport, we estimated the effective mass (m^*) and carrier mobility (μ) of the proposed systems. Using the conventional definition [69], the m^* of electrons and holes are predicted by the quadratic fitting of the electronic band structure with the following expression: $m^* = \hbar(d^2E(k)/dk^2)^{-1}$ where $\hbar$ is the reduced Planck constant, k is wave-vector and $E(k)$ is the energy with respect to k. Considering the dissimilarity in dispersion throughout the Γ-X and Γ-Y, m^* values of electrons and holes are calculated for x- and y-directions and listed in Table 3. The resultant values exhibit a high degree of anisotropy in m^*, which is compatible with the difference in electronic band dispersions along with both directions. In general, electrons have smaller values of m^* compared to holes, which allows electrons and holes to be spatially discretized. On the other hand, the direction-dependent differences in the m^* values are also favorable for efficient carrier transport. Further, we calculated μ in the deformation potential theory (DPT) framework, which is based on the fact that atomic displacement caused by a long-wavelength acoustic phonon perturbs the crystal and modulates the

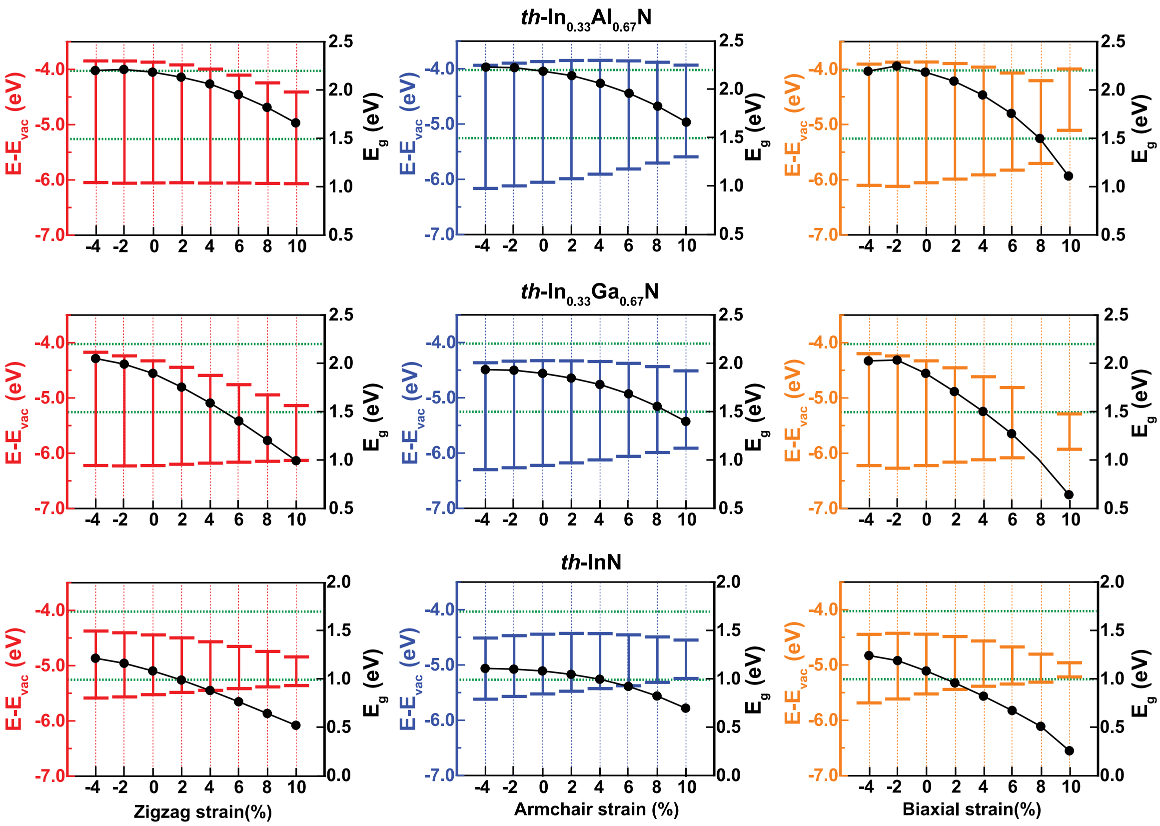

Fig. 8. The electronic band gaps (black circles) and band edge positions (pink, blue, and orange colors for uniaxial-x (zigzag), uniaxial-y (armchair), and biaxial strains, respectively) of 2D th-$In_{0.33}X_{0.67}N$ with respect to the vacuum level under strain from −4% to +10% (negative/positive numbers denotes the compressive/tensile strains) calculated with HSE06. The upper and lower horizontal solid lines represent the positions of the CBM and the VBM, respectively. The redox potential of water splitting is shown in a green dashed line for pH = 7.

Table 3
Carrier effective mass m^* (m_0 is the mass of free electrons) along Γ–X and Γ–Y directions, deformation potential constant E_d in eV, and carrier mobility μ in ($cm^2/(V.s)$) of th-$In_{0.33}X_{0.67}N$ (X = Al, Ga, In) monolayers along the x- and y-directions.

		m_x^*/m_0	m_y^*/m_0	m_d^*/m_0	C_x	C_y	E_d^x	E_d^y	$\mu_x(\times 10^3)$	$\mu_y(\times 10^3)$
th-$In_{0.33}Al_{0.67}N$	electron	0.33	0.78	0.51	88.14	60.41	0.38	3.39	3.51	0.67
	hole	2.18	1.81	1.98	88.14	60.41	1.59	1.33	0.17	0.21
th-$In_{0.33}Ga_{0.67}N$	electron	0.23	0.79	0.43	75.40	53.53	0.93	2.29	6.68	1.19
	hole	8.16	1.77	3.80	75.40	53.53	5.38	0.17	~0.01	0.03
th-InN	electron	0.25	0.84	0.46	59.46	41.83	0.29	0.41	86.85	19.98
	hole	2.72	0.84	1.52	59.56	41.83	4.03	0.93	0.03	0.16

electronic band dispersion [70,71]. DPT can therefore be used to reflect the fundamental charge-transport features of semiconducting devices adequately. μ of electrons and holes can be predicted along with both directions according to the given formula by taking into account the anisotropy in deformation potential [71]:

$$\mu_i = \frac{e\hbar^3\left(\frac{5C_i+3C_j}{8}\right)}{k_B T (m_i^*)^{3/2}(m_j^*)^{1/2}\left(\frac{9E_{d,i}^2+7E_{d,i}E_{d,j}+4E_{d,j}^2}{20}\right)} \tag{7}$$

where $C_{i,j}$ is the elastic constant of corresponding direction (x- or y-directions), k_B is the Boltzmann's constant, T is the room temperature (300 K), and $E_{d,(i,j)}$ is the deformation potential constant. E_d is determined by imposing minute tensile and compressive strains in both directions to simulate lattice deformation driven by phonons. It should be noted that DPT provides the upper value of mobility since it only considers the electron–phonon coupling, while other interactions are not taken into account. We plotted the overall energy changes of VBM and CBM as a function of compressive and tensile strain for all monolayers (Figure S7), in which the slopes of the straight lines found by linear fitting correspond to the E_d. The calculated μ values are summarized in Table 3 and they are found to be highly direction and carrier type dependent. While μ of holes are calculated to be very low, μ of electrons for th-$In_{0.33}X_{0.67}N$ monolayers are order of magnitude larger than the MoS_2 [72]. Moreover, obtained electron mobility of 2D th-InN (86.85 × 10^3 $cm^2/(V\ s)$) is within the same range of th-GeC_2 (90.53 × 10^3 $cm^2/(V\ s)$) which have been proposed recently to have ultrahigh carrier mobility [20]. On the other hand, as alloying can result in dramatic decrease in charge carrier mobilities, a significant reduction in electron mobility is noticed for th-$Ga_{0.33}X_{0.67}N$ and th-$Al_{0.33}X_{0.67}N$ monolayers. We also examined the effect of anisotropy on the carrier mobility and calculated μ values without considering the anisotropy in deformation potential, effective mass, and elastic constants using Bardeen-Shockley's formula [70] in Table S1. It should be also noted that the presented electronic properties and band alignment scheme can only provide a simple picture of the photocatalytic water splitting applications, and additional analyses are required to reveal the full potential [73].

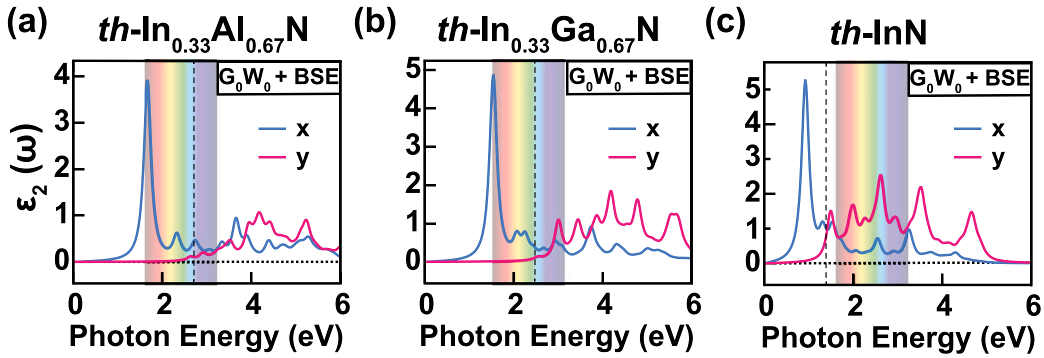

Fig. 9. The polarization components (blue for x- and pink for y-directions) of the imaginary part of the complex dielectric function $\varepsilon_2(\omega)$ as a function of the photon energy calculated using G_0W_0 + BSE method for (a) *th*-$In_{0.33}Al_{0.67}N$ (b) *th*-$In_{0.33}Ga_{0.67}N$, and (c) *th*-InN monolayers. The band gap at the level of GW is denoted by the vertical dashed line.

3.5. Optical properties

Aside from appropriate band positions, a moderate band gap, and anisotropic high μ values, a photocatalyst's light absorption capacity is a significant element in real-world applications. This can be evaluated by the evolution of the imaginary part of the complex dielectric function ($\varepsilon_2(\omega)$) with respect to photon energy since $\varepsilon_2(\omega)$ is directly related to the absorption coefficient. Due to the quantum confinement effects and weak intrinsic screening, 2D materials are expected to have strong excitonic effects. Thus, it is crucial to accurately calculate the optical response of proposed monolayers considering many-body effects, including electron–electron and electron–hole interactions. In this respect, we determined the optical response by employing the Bethe–Salpeter equation (BSE) on top of the self-consistent single-shot G_0W_0 calculation. The modulation of $\varepsilon_2(\omega)$ with respect to photon energy for both polarization components can be seen in Fig. 9. The quasi-particle G_0W_0 band gaps are calculated as 2.61, 2.36, and 1.28 eV for *th*-$In_{0.33}Al_{0.67}N$, *th*-$In_{0.33}Ga_{0.67}N$ and *th*-InN, respectively. When excitonic effects are included by solving BSE, the first and prominent absorption peaks in the spectrum of all monolayers are observed for light polarization along x- and y-directions. The locations of these absorption peaks are 1.66, 1.54, and 0.92 eV by which the corresponding exciton binding energies are calculated as 950, 820, and 360 meV for *th*-$In_{0.33}Al_{0.67}N$, *th*-$In_{0.33}Ga_{0.67}N$ and *th*-InN, respectively. The decrease in exciton binding energy can be correlated with the increase in dielectric screening [74], and the narrowing of the band gap [75]. Additional exciton peaks are noticed at 2.34 eV for *th*-$In_{0.33}Al_{0.67}N$, at 2.11 and 2.26 eV for *th*-$In_{0.33}Ga_{0.67}N$, and at 1.33 eV for *th*-InN. Since third exciton peaks of *th*-$In_{0.33}Al_{0.67}N$ and *th*-InN are located in the GW band gap, they can be considered as unbound excitons. It should be noted that both pristine and alloyed structures exhibit highly anisotropic optical behavior. The exciton formation for all the monolayers can only be monitored when the polarization direction of the incident beam is parallel to the x-direction. This direction-dependent feature can be attributed to structural anisotropy and offers an additional degree of freedom for device design which can be exploited in angle-dependent optical and optoelectronic applications.

4. Conclusions

In summary, motivated by the recent theoretical findings in *h*-InN and 2D *th*-materials, we have computationally designed *th*-$In_{0.33}X_{0.67}N$ (X = Al, Ga, In) monolayers and explored their unique properties which can be utilized particularly in photocatalytic water splitting applications. We have shown that *th*-$In_{0.33}X_{0.67}N$ systems are energetically and dynamically stable and maintain their overall integrity even at high temperatures. The structural anisotropy gives rise to direction-dependent mechanical properties, and computed low Young's modulus values, which increase with alloying, indicate that the studied monolayers are elastic. Additionally, they exhibit half-auxetic character under applied tensile strain. While pristine *th*-InN monolayer has an indirect band gap within the infrared region (1.08 eV), the inclusion of Al and Ga widens the band gap and shifts it to the visible part (up to 2.19 eV). The modified band gaps, together with ideal band edge positions especially make *th*-$In_{0.33}Al_{0.67}N$ ideal system for photocatalytic water splitting. Furthermore, the charge carrier mobilities are found to be extremely anisotropic and high (for electrons), which is critical to boosting the catalytic performance of these crystals. The optical absorbance capacity of the proposed materials is found to be significant in the visible and UV part of the spectrum with strong excitonic effects (i.e., multiple bound excitons with very high binding energies). These excellent and tunable properties render the 2D *th*-InN and its alloys promising materials for electronic and optical applications at the nanoscale and peculiarly highlight them as a photocatalyst that can perform efficiently in water-splitting reactions.

CRediT authorship contribution statement

Dogukan Hazar Ozbey: Conceptualization, Investigation, Writing – original draft, Writing – review & editing, Visualization. **Mehmet Emin Kilic:** Supervision, Writing – review & editing. **Engin Durgun:** Supervision, Writing – review & editing.

Declaration of competing interest

The authors declare that they have no known competing financial interests or personal relationships that could have appeared to influence the work reported in this paper.

Data availability

No data was used for the research described in the article.

Acknowledgments

This work was supported by the Scientific and Technological Research Council of Turkey (TUBITAK) under Project No. 121F126. The calculations were performed at TUBITAK ULAKBIM, High Performance and Grid Computing Center (TR-Grid e-Infrastructure), and the National Center for High-Performance Computing of Turkey (UHeM) under grant no. 5007092019. M.E.K acknowledges support from Brain Pool Program through the National Research Foundation of Korea (NRF), funded by the Ministry of Science and ICT (2020H1D3A1A0208 1517).

Appendix A. Supplementary data

Supplementary material related to this article can be found online at https://doi.org/10.1016/j.apsusc.2023.157982.

References

[1] K.S. Novoselov, A.K. Geim, S.V. Morozov, D. Jiang, Y. Zhang, S.V. Dubonos, I.V. Grigorieva, A.A. Firsov, Electric field effect in atomically thin carbon films, Science 306 (5696) (2004) 666–669.
[2] K.S. Novoselov, A.K. Geim, S.V. Morozov, D. Jiang, M.I. Katsnelson, I. Grigorieva, S. Dubonos, Firsov, Two-dimensional gas of massless Dirac fermions in graphene, Nature 438 (7065) (2005) 197–200.
[3] Y. Liu, N.O. Weiss, X. Duan, H.-C. Cheng, Y. Huang, X. Duan, Van der Waals heterostructures and devices, Nat. Rev. Mater. 1 (9) (2016) 16042.
[4] F. Ersan, D. Keçik, V. Özçelik, Y. Kadioglu, O.Ü. Aktürk, E. Durgun, E. Aktürk, S. Ciraci, Two-dimensional pnictogens: A review of recent progresses and future research directions, Appl. Phys. Rev. 6 (2) (2019) 021308.
[5] F.A. Rasmussen, K.S. Thygesen, Computational 2D materials database: Electronic structure of transition-metal dichalcogenides and oxides, J. Phys. Chem. C 119 (23) (2015) 13169–13183.
[6] S. Manzeli, D. Ovchinnikov, D. Pasquier, O.V. Yazyev, A. Kis, 2D transition metal dichalcogenides, Nat. Rev. Mater. 2 (8) (2017) 17033.
[7] N. Mounet, M. Gibertini, P. Schwaller, D. Campi, A. Merkys, A. Marrazzo, T. Sohier, I.E. Castelli, A. Cepellotti, G. Pizzi, N. Marzari, Two-dimensional materials from high-throughput computational exfoliation of experimentally known compounds, Nat. Nanotechnol. 13 (3) (2018) 246–252.
[8] H. Lu, S.-D. Li, Two-dimensional carbon allotropes from graphene to graphyne, J. Mater. Chem. C 1 (23) (2013) 3677–3680.
[9] V. Georgakilas, J.A. Perman, J. Tucek, R. Zboril, Broad family of carbon nanoallotropes: Classification, chemistry, and applications of fullerenes, carbon dots, nanotubes, graphene, nanodiamonds, and combined superstructures, Chem. Rev. 115 (11) (2015) 4744–4822.
[10] Y. Chen, Y. Xie, X. Yan, M.L. Cohen, S. Zhang, Topological carbon materials: A new perspective, Phys. Rep. 868 (2020) 1–32.
[11] B. Sarikavak-Lisesivdin, S. Lisesivdin, E. Ozbay, F. Jelezko, Structural parameters and electronic properties of 2D carbon allotrope: Graphene with a kagome lattice structure, Chem. Phys. Lett. 760 (2020) 138006.
[12] S. Zhang, J. Zhou, Q. Wang, X. Chen, Y. Kawazoe, P. Jena, Penta-graphene: A new carbon allotrope, Proc. Natl. Acad. Sci. 112 (8) (2015) 2372–2377.
[13] B. Ram, H. Mizuseki, Tetrahexcarbon: A two-dimensional allotrope of carbon, Carbon 137 (2018) 266–273.
[14] M.E. Kilic, K.-R. Lee, Tuning the electronic, mechanical, thermal, and optical properties of tetrahexcarbon via hydrogenation, Carbon 161 (2020) 71–82.
[15] M.E. Kilic, K.-R. Lee, Novel two-dimensional group-IV carbides containing C2 dimers: Sizable direct band gap, high carrier mobility, and anisotropic properties for nanoelectronics, Carbon 181 (2021) 421–432.
[16] C. Lee, X. Wei, J.W. Kysar, J. Hone, Measurement of the elastic properties and intrinsic strength of monolayer graphene, Science 321 (5887) (2008) 385–388.
[17] Q. Wei, Y. Yang, A. Gavrilov, X. Peng, A new 2D auxetic CN2 nanostructure with high energy density and mechanical strength, Phys. Chem. Chem. Phys. 23 (7) (2021) 4353–4364.
[18] M.E. Kilic, K.-R. Lee, Tetrahex carbides: Two-dimensional group-IV materials for nanoelectronics and photocatalytic water splitting, Carbon 174 (2021) 368–381.
[19] M.E. Kilic, S.E. Rad, S. Jahangirov, Two-dimensional tetrahexagonal C X 2 (X=P, As, Sb) semiconductors for photocatalytic water splitting under visible light, Phys. Rev. Mat. 6 (3) (2022) 035402.
[20] W. Zhang, C. Chai, Q. Fan, M. Sun, Y. Song, Y. Yang, U. Schwingenschlogl, Two-dimensional tetrahex-GeC2: A material with tunable electronic and optical properties combined with ultrahigh carrier mobility, ACS Appl. Mater. Interfaces 13 (12) (2021) 14489–14496.
[21] W. Wu, D. Li, Y. Xu, X.C. Zeng, Two-dimensional GeC2 with tunable electronic and carrier transport properties and a high current ON/OFF ratio, J. Phys. Chem. Lett. 12 (47) (2021) 11488–11496.
[22] M.E. Kilic, K.-R. Lee, Novel two-dimensional tetrahexagonal boron nitride with a sizable band gap and a sign-tunable Poisson's ratio, Nanoscale 13 (20) (2021) 9303–9314.
[23] M.E. Kilic, K.-R. Lee, Auxetic, flexible, and strain-tunable two-dimensional th-AlN for photocatalytic visible light water splitting with anisotropic high carrier mobility, J. Mater. Chem. C 9 (14) (2021) 4971–4977.
[24] D. Liang, R. Quhe, Y. Chen, L. Wu, Q. Wang, P. Guan, S. Wang, P. Lu, Electronic and excitonic properties of two-dimensional and bulk InN crystals, RSC Adv. 7 (67) (2017) 42455–42461.
[25] G. Kresse, J. Hafner, Ab initio molecular dynamics for liquid metals, Phys. Rev. B 47 (1) (1993) 558.
[26] G. Kresse, J. Hafner, Ab initio molecular-dynamics simulation of the liquid-metal–amorphous-semiconductor transition in germanium, Phys. Rev. B 49 (20) (1994) 14251.
[27] G. Kresse, J. Furthmüller, Efficiency of ab initio total energy calculations for metals and semiconductors using a plane-wave basis set, Comput. Mater. Sci. 6 (1) (1996) 15–50.
[28] G. Kresse, J. Furthmüller, Efficient iterative schemes for ab initio total-energy calculations using a plane-wave basis set, Phys. Rev. B 54 (16) (1996) 11169.
[29] G. Kresse, D. Joubert, From ultrasoft pseudopotentials to the projector augmented-wave method, Phys. Rev. B 59 (3) (1999) 1758.
[30] P.E. Blöchl, Projector augmented-wave method, Phys. Rev. B 50 (24) (1994) 17953.
[31] J.P. Perdew, K. Burke, M. Ernzerhof, Generalized gradient approximation made simple, Phys. Rev. Lett. 77 (18) (1996) 3865.
[32] J. Heyd, G.E. Scuseria, M. Ernzerhof, Hybrid functionals based on a screened Coulomb potential, J. Chem. Phys. 118 (18) (2003) 8207–8215.
[33] J. Paier, M. Marsman, K. Hummer, G. Kresse, I.C. Gerber, J.G. Ángyán, Screened hybrid density functionals applied to solids, J. Chem. Phys. 124 (15) (2006) 154709.
[34] A. Togo, I. Tanaka, First principles phonon calculations in materials science, Scr. Mater. 108 (2015) 1–5.
[35] S. Nosé, A molecular dynamics method for simulations in the canonical ensemble, Mol. Phys. 52 (2) (1984) 255–268.
[36] H. Ehrenreich, M.H. Cohen, Self-consistent field approach to the many-electron problem, Phys. Rev. 115 (4) (1959) 786.
[37] M. Shishkin, G. Kresse, Implementation and performance of the frequency-dependent GW method within the PAW framework, Phys. Rev. B 74 (3) (2006) 035101.
[38] E.E. Salpeter, H.A. Bethe, A relativistic equation for bound-state problems, Phys. Rev. 84 (6) (1951) 1232.
[39] G. Onida, L. Reining, A. Rubio, Electronic excitations: density-functional versus many-body Green's-function approaches, Rev. Modern Phys. 74 (2) (2002) 601.
[40] H.-P. Komsa, S. Kurasch, O. Lehtinen, U. Kaiser, A.V. Krasheninnikov, From point to extended defects in two-dimensional MoS2: Evolution of atomic structure under electron irradiation, Phys. Rev. B 88 (3) (2013) 035301.
[41] G. Li, Y. Li, H. Liu, Y. Guo, Y. Li, D. Zhu, Architecture of graphdiyne nanoscale films, Chem. Commun. 46 (19) (2010) 3256–3258.
[42] M. Born, K. Huang, Dynamical Theory of Crystal Lattices, Clarendon press, Oxford, UK, 1954.
[43] L. Wang, A. Kutana, X. Zou, B.I. Yakobson, Electro-mechanical anisotropy of phosphorene, Nanoscale 7 (21) (2015) 9746–9751.
[44] E. Cadelano, P.L. Palla, S. Giordano, L. Colombo, Elastic properties of hydrogenated graphene, Phys. Rev. B 82 (23) (2010) 235414.
[45] P. Hess, Bonding, structure, and mechanical stability of 2D materials: the predictive power of the periodic table, Nanoscale Horiz. 6 (11) (2021) 856–892.
[46] R.M. Christensen, Mechanisms and measures for the ductility of materials failure, Proc. Math. Phys. Eng. Sci. 476 (2239) (2020) 20190719.
[47] S. Burns, Negative Poisson's ratio materials, Science 238 (4826) (1987) 551.
[48] R. Peng, Y. Ma, Z. He, B. Huang, L. Kou, Y. Dai, Single-layer Ag2S: a two-dimensional bidirectional auxetic semiconductor, Nano Lett. 19 (2) (2019) 1227–1233.
[49] L. Kou, Y. Ma, C. Tang, Z. Sun, A. Du, C. Chen, Auxetic and ferroelastic borophane: a novel 2D material with negative possion's ratio and switchable dirac transport channels, Nano Lett. 16 (12) (2016) 7910–7914.
[50] J.-W. Jiang, H.S. Park, Negative Poisson's ratio in single-layer black phosphorus, Nature Commun. 5 (1) (2014) 4727.
[51] Z. Gao, Q. Wang, W. Wu, Z. Tian, Y. Liu, F. Ma, Y. Jiao, S.A. Yang, Monolayer RhB4: Half-auxeticity and almost ideal spin-orbit Dirac point semimetal, Phys. Rev. B 104 (24) (2021) 245423.
[52] F. Ma, Y. Jiao, W. Wu, Y. Liu, S.A. Yang, T. Heine, Half-auxeticity and anisotropic transport in Pd decorated two-dimensional boron sheets, Nano Lett. 21 (6) (2021) 2356–2362.
[53] M.E. Kilic, K.-R. Lee, Four-penta-graphenes: Novel two-dimensional fenestrane-based auxetic nanocarbon allotropes for nanoelectronics and optoelectronics, Carbon 195 (2022) 154–164.
[54] D.T. Ho, S.-D. Park, S.-Y. Kwon, K. Park, S.Y. Kim, Negative Poisson's ratios in metal nanoplates, Nature Commun. 5 (1) (2014) 1–8.
[55] J.-W. Jiang, H.S. Park, Negative Poisson's ratio in single-layer graphene ribbons, Nano Lett. 16 (4) (2016) 2657–2662.
[56] B. Deng, J. Hou, H. Zhu, S. Liu, E. Liu, Y. Shi, Q. Peng, The normal-auxeticity mechanical phase transition in graphene, 2D Mater. 4 (2) (2017) 021020.
[57] J. Wu, E. Zhou, Z. Qin, X. Zhang, G. Qin, Accessing negative Poisson's ratio of graphene by machine learning interatomic potentials, Nanotechnology 33 (27) (2022) 275710.
[58] G. Wang, W. Tang, W. Xie, Q. Tang, Y. Wang, H. Guo, P. Gao, S. Dang, J. Chang, Type-II CdS/PtSSe heterostructures used as highly efficient water-splitting photocatalysts, Appl. Surf. Sci. 589 (2022) 152931.
[59] S.-S. Cui, X. Liu, Y.-B. Shi, M.-Y. Ding, X.-F. Yang, Construction of atomic-level charge transfer channel in Bi12O17Cl2/MXene heterojunctions for improved visible-light photocatalytic performance, Rare Metals 41 (7) (2022) 2405–2416.
[60] L. Ye, X. Peng, Z. Wen, H. Huang, Solid-state Z-scheme assisted hydrated tungsten trioxide/ZnIn2S4 photocatalyst for efficient photocatalytic H2 production, Mater. Futures 1 (3) (2022) 035103.

[61] M. Jakhar, A. Kumar, P.K. Ahluwalia, K. Tankeshwar, R. Pandey, Engineering 2D materials for photocatalytic water-splitting from a theoretical perspective, Materials 15 (6) (2022) 2221.
[62] M. Jakhar, A. Kumar, Two-dimensional β-PdX 2 (X=S, Te) monolayers for efficient solar energy conversion applications, J. Mater. Chem. A 10 (12) (2022) 6785–6795.
[63] P. Jamdagni, A. Kumar, S. Srivastava, R. Pandey, K. Tankeshwar, Photocatalytic properties of anisotropic β-PtX 2 (X=S, Se) and Janus β-PtSSe monolayers, Phys. Chem. Chem. Phys. 24 (36) (2022) 22289–22297.
[64] V. Chakrapani, J.C. Angus, A.B. Anderson, S.D. Wolter, B.R. Stoner, G.U. Sumanasekera, Charge transfer equilibria between diamond and an aqueous oxygen electrochemical redox couple, Science 318 (5855) (2007) 1424–1430.
[65] J. Greeley, T.F. Jaramillo, J. Bonde, I. Chorkendorff, J.K. Nørskov, Computational high-throughput screening of electrocatalytic materials for hydrogen evolution, Nature Mater. 5 (11) (2006) 909–913.
[66] J.K. Nørskov, T. Bligaard, A. Logadottir, J. Kitchin, J.G. Chen, S. Pandelov, U. Stimming, Trends in the exchange current for hydrogen evolution, J. Electrochem. Soc. 152 (3) (2005) J23.
[67] C. Long, Y. Liang, H. Jin, B. Huang, Y. Dai, PdSe2: flexible two-dimensional transition metal dichalcogenides monolayer for water splitting photocatalyst with extremely low recombination rate, ACS Appl. Energy Mater. 2 (1) (2018) 513–520.
[68] L. Ju, M. Bie, X. Tang, J. Shang, L. Kou, Janus WSSe monolayer: an excellent photocatalyst for overall water splitting, ACS Appl. Mater. Interfaces 12 (26) (2020) 29335–29343.
[69] N.W. Ashcroft, N.D. Mermin, et al., Solid state physics, 1976.
[70] J. Bardeen, W. Shockley, Deformation potentials and mobilities in non-polar crystals, Phys. Rev. 80 (1) (1950) 72.
[71] H. Lang, S. Zhang, Z. Liu, Mobility anisotropy of two-dimensional semiconductors, Phys. Rev. B 94 (23) (2016) 235306.
[72] B. Radisavljevic, A. Radenovic, J. Brivio, V. Giacometti, A. Kis, Single-layer MoS2 transistors, Nat. Nanotechnol. 6 (3) (2011) 147–150.
[73] J.K. Nø rskov, J. Rossmeisl, A. Logadottir, L. Lindqvist, J.R. Kitchin, T. Bligaard, H. Jonsson, Origin of the overpotential for oxygen reduction at a fuel-cell cathode, J. Phys. Chem. B 108 (46) (2004) 17886–17892.
[74] J. Pei, J. Yang, T. Yildirim, H. Zhang, Y. Lu, Many-body complexes in 2D semiconductors, Npj 2D Mater. Appl. 31 (2) (2019) 1706945.
[75] Z. Jiang, Z. Liu, Y. Li, W. Duan, Scaling universality between band gap and exciton binding energy of two-dimensional semiconductors, Phy. Rev. Lett. 118 (26) (2017) 266401.